Research Square

Preprints are preliminary reports that have not undergone peer review.
They should not be considered conclusive, used to inform clinical practice,
or referenced by the media as validated information.

Electrochemical Capture of U(VI) by Fe/Fe3O4@PPy Core–Shell Nanocomposites via Synergistic Adsorption and Reductive Immobilization

Yating Fu
East China University of Technology
Yi Zhao
East China University of Technology
Xiang Zhou
East China University of Technology
Chunpei Yan
East China University of Technology
Chunyan Wang
East China University of Technology
Tianxiang Jin
20166027@ecut.edu.cn
East China University of Technology

Research Article

Keywords: Polypyrrole, Core–shell nanocomposite, Ferroferric oxide, Uranium

Posted Date: November 24th, 2026

DOI: https://doi.org/10.21203/rs.3.rs-11570577/v1

License: This work is licensed under a Creative Commons Attribution 4.0 International License.
Read Full License

Additional Declarations: No competing interests reported.

Electrochemical Capture of U(VI) by Fe/Fe_3O_4@PPy Core–Shell Nanocomposites via Synergistic Adsorption and Reductive Immobilization

Yating Fu, Yi Zhao, Xiang Zhou, Chunpei Yan*, Chunyan Wang, Tianxiang Jin*

National Key Laboratory of Uranium Resources Exploration–Mining and Nuclear Remote Sensing, East China University of Technology, Nanchang, 330013, China

Corresponding authors.

E-mail addresses: 201660027@ecut.edu.cn (T. Jin),

ycp201960012@ecut.edu.cn (Y. Pei)

Abstract: Efficient separation and immobilization of uranium from dilute aqueous environments remain challenging due to the low concentration and complex composition of uranium-containing wastewater. Herein, Fe/Fe_3O_4@PPy core–shell nanocomposites were synthesized through an oxidative polymerization–in situ reduction strategy for electrochemical capture and immobilization of U(VI). The polypyrrole shell effectively stabilized the iron-based components and generated a porous structure, while the Fe/Fe_3O_4 core provided electron-transfer sites for U(VI) reduction. The optimized Fe/Fe_3O_4@PPy-2 electrode exhibited a high U(VI) electrosorption capacity of 735.57 mg g^{-1} at pH 7, with a maximum capacity of 1208.6 mg g^{-1} according to the Langmuir model. The adsorption kinetics and isotherm analyses indicated that uranium capture involved surface chemical interactions and monolayer adsorption. In addition, Fe/Fe_3O_4@PPy-2 showed high selectivity toward U(VI) in the presence of competing metal ions, with a uranium distribution coefficient of 2.08×10^4 mL g^{-1}, and maintained 84.22% of its initial capacity after five regeneration cycles. Mechanistic investigations revealed that U(VI) was captured through the synergistic effects of surface coordination and reductive immobilization, where Fe^0 acted as an electron donor to partially reduce U(VI) into insoluble U(IV) species, while the PPy/Fe_3O_4 interface facilitated uranium enrichment. This work provides a strategy for designing stable iron-based core–shell materials for electrochemical uranium recovery and wastewater remediation.

Article Highlights

Porous iron–polypyrrole electrodes enable electrochemical uranium capture.

Uranium uptake reaches 735.57 mg g^{-1} at neutral pH.

Surface binding and partial reduction work together to immobilize uranium.

Keywords: Polypyrrole; Core–shell nanocomposite; Ferroferric oxide; Uranium

1. Introduction

With the rapid development of nuclear energy, the treatment of uranium-containing wastewater and the recycling and recovery of uranium resources have become important topics in the fields of environmental science and the nuclear fuel cycle. In aqueous solution, uranium exists predominantly in the form of hexavalent uranyl ions [U(VI)], which possess high solubility and mobility and thus pose a potential threat to the ecological environment and human health. The reduction of soluble U(VI) to sparingly soluble U(IV) (e.g., UO_2 precipitates) is one of the most effective strategies for uranium immobilization and recovery.[1, 2]

Electrochemical reduction has attracted extensive attention owing to its advantages of controllable reaction, high efficiency, and the absence of additional chemical reducing agents.[3-5]Among the numerous electrode materials, zero-valent iron (Fe^0) is regarded as an ideal material for the reduction of U(VI) owing to its strong reducing capability, environmental friendliness, and low cost.[6] However, nanoscale zero-valent iron faces two major bottlenecks in practical applications: first, nanoparticles are highly prone to aggregation, leading to a sharp decrease in the effective reactive area; second, a passivation layer (iron (hydr)oxides) rapidly forms on the Fe^0 surface during the reaction, which blocks electron transfer and severely restricts its reduction efficiency.[6, 7]

Polypyrrole (PPy), as a conducting polymer with good electrical conductivity and environmental stability, has been employed to coat zero-valent iron nanoparticles in order to suppress their aggregation and surface oxidation.[8, 9]However, systematic studies on the mechanism of Fe/PPy composites in the electrochemical reduction of

U(VI) remain scarce. In this study, Fe/Fe_3O_4@PPy core-shell structured composites were synthesized via a two-step "oxidative polymerization-in situ reduction" method under nitrogen protection, and their performance for U(VI) removal was systematically investigated.[10] The proposed removal mechanism involves the surface complexation and enrichment of U(VI) by the nitrogen-containing functional groups of the PPy shell, together with an electron transfer process in which Fe(0)/Fe(II) reduces U(VI) to U(IV) (UO_2); meanwhile, part of the U(VI) may precipitate on the material surface in the form of $UO_3 \cdot 2H_2O$.[11] The introduction of nitrogen protection is intended to ensure the stable formation and preservation of Fe^0 during synthesis, thereby enabling the zero-valent iron in the material to enable Fe^0 to participate in U(VI) reduction, and providing an alternative approach for electrochemical uranium remediation.

2. Synthesis of Fe/Fe_3O_4@PPy

First, 5.93 g of $FeCl_3 \cdot 6H_2O$ was dissolved in 40 mL of deionized water and transferred to a 250 mL three-neck flask. Under magnetic stirring, 0.6 mL of Py was slowly added dropwise to the above solution, and the mixture was kept under continuous stirring in an ice-water bath (5–7℃). High-purity nitrogen was introduced throughout the reaction to maintain an inert atmosphere. After the reaction had proceeded for a period of time, 100 mL of freshly prepared $NaBH_4$ solution was added dropwise, and the stirring was continued for another 30 min. After the reaction, the product was separated by vacuum filtration, washed three times with deionized water and anhydrous ethanol, respectively, and then dried in a freeze dryer to obtain a black powdery product. Following the same procedure as above, two other Fe/Fe_3O_4@PPy composites with different $FeCl_3$-to-Py molar ratios of 1:0.2 and 1:0.6 were synthesized. The resulting materials were designated as Fe/Fe_3O_4@PPy-1, Fe/Fe_3O_4@PPy-2, and Fe/Fe_3O_4@PPy-3, respectively. The detailed synthesis route and parameters are summarized in Scheme 1 and Table S1, respectively. Among them, Fe/Fe_3O_4@PPy-2 was selected as the typical material for the systematic investigation of the U(VI) adsorption mechanism.

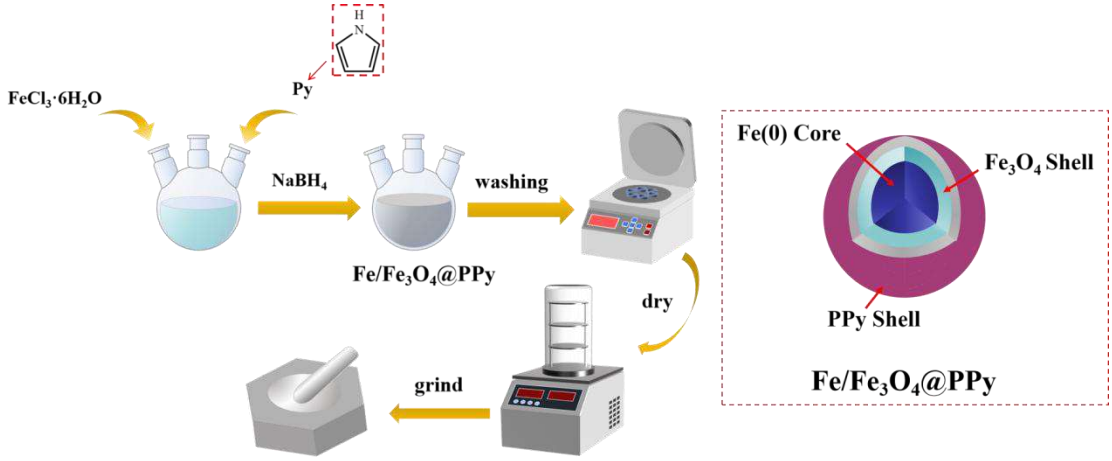

Scheme 1. Schematic illustration of the synthetic route for Fe/Fe_3O_4@PPy.

The detailed characterization methods and electrochemical measurements are provided in the Supporting Information.

3 Results and discussion

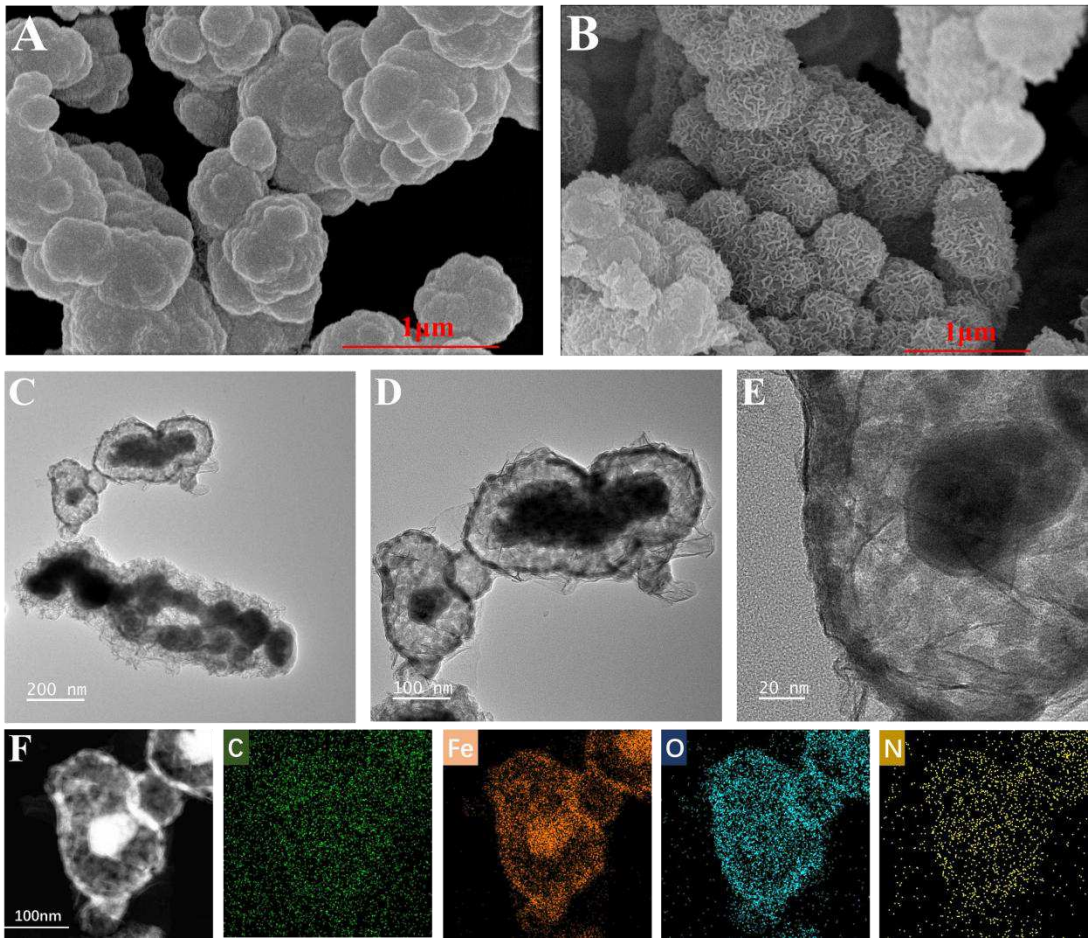

Fig. 1. (A) SEM image of PPy; (B) SEM image of Fe/Fe_3O_4@PPy-2 before adsorption; (C-E) TEM images of Fe/Fe_3O_4@PPy-2 before adsorption at different magnifications; (F) TEM-EDS elemental mapping images of Fe/Fe_3O_4@PPy-2 before adsorption.

The microscopic morphology and elemental distribution of the Fe/Fe_3O_4@PPy-2 composite were characterized by SEM, TEM, and TEM-EDS elemental mapping. The SEM results showed that PPy, obtained by oxidative polymerization of Py with $FeCl_3$ (Fig. 1A), exhibited quasi-spherical particles with a relatively dense and smooth surface. After further reduction treatment with sodium borohydride, the resulting Fe/Fe_3O_4@PPy-2 (Fig. 1B) largely retained the quasi-spherical outline, while a unique flower-like porous structure formed on the surface. This structure originated from the hydrogen gas released during the reduction process, whose escape created abundant pores in the polypyrrole surface layer. TEM images at different magnifications (Fig. 1C, 1D, 1E) confirmed that the sample possessed a typical multilayer core-shell structure: the inner region of high contrast and dark appearance corresponded to zero-valent iron (Fe^0), the thin light-black layer adjacent to the outer surface of Fe^0 was the Fe_3O_4 oxide layer, and the outermost layer was a loose, flocculent polypyrrole (PPy) coating. TEM-EDS elemental mapping of a selected local region (Fig. 1F) revealed that C and N were uniformly distributed throughout the entire particle, corresponding to the outer PPy matrix; Fe was markedly enriched at the particle center, consistent with the position of the Fe^0 core; and O was mainly distributed in the peripheral region of the Fe core, further corroborating the presence of the Fe_3O_4 oxide layer.[12, 13] The above characterization results demonstrate that the Fe/Fe_3O_4@PPy core-shell composite was successfully prepared, and that its rough, porous surface and hierarchical core-shell structure can expose more active sites, which is expected to enhance the adsorption performance of the material.

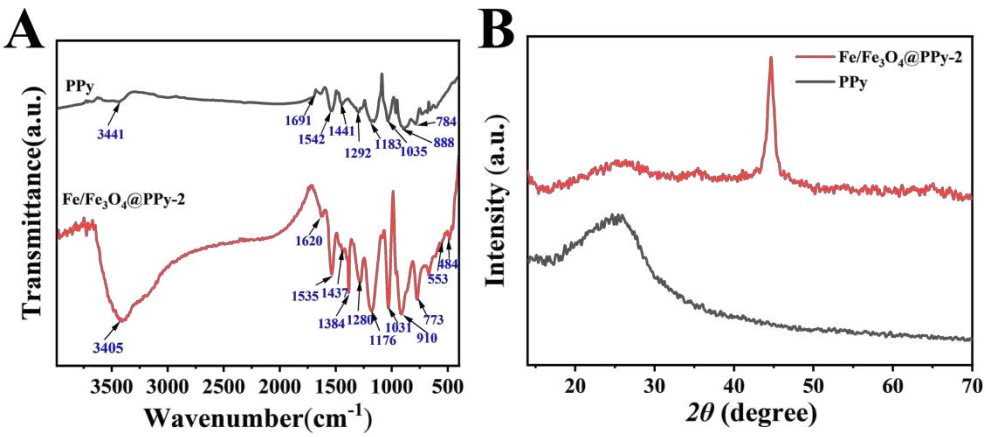

Fig. 2. (A) FT-IR spectra of PPy and Fe/Fe_3O_4@PPy-2; (B) XRD patterns of PPyand Fe/Fe_3O_4@PPy-2before adsorption.

FT-IR spectroscopy was employed to characterize the surface functional groups of PPy and the Fe/Fe_3O_4@PPy composites, and to analyze the interaction between the polypyrrole backbone and the iron oxides. As shown in Fig. 2A, pristine PPy exhibited characteristic absorption peaks at 3441 cm^{-1}, 1691 cm^{-1}, and 1542 cm^{-1}, which were assigned to N–H stretching vibration, C–N stretching vibration, and asymmetric C–C stretching vibration of the pyrrole ring, respectively. The absorption peaks at 1441 cm^{-1}, 1292 cm^{-1}, 1183 cm^{-1}, 1035 cm^{-1}, 888 cm^{-1}, and 784 cm^{-1} corresponded to symmetric stretching vibration of the pyrrole ring, C–C bond vibration, conjugated C–N stretching vibration, in-plane bending vibration of =C–H, in-plane deformation vibration of N–H, and out-of-plane bending vibration of C–H, respectively[14, 15]. Compared with pristine PPy, the PPy-related characteristic peaks in Fe/Fe_3O_4@PPy-2 exhibited an obvious red shift along with increased absorption intensity, indicating the existence of interactions between the iron-based components and the PPy molecular chains. Meanwhile, new absorption signals appeared at 1384 cm^{-1}, 553 cm^{-1}, and 484 cm^{-1}, among which the bands at 553 cm^{-1} and 484 cm^{-1} were attributed to Fe–O stretching vibration, confirming the presence of Fe_3O_4, while the peak at 1384 cm^{-1} originated from the O–H bending vibration of water molecules adsorbed on the material surface[16, 17]. It should be noted that metallic Fe^0 is infrared-inactive and has no characteristic absorption in the infrared region; therefore,

FT-IR cannot directly confirm the presence of zero-valent iron.Figure2B XRD characterization analysis of the crystal structureand phase composition of PPy and Fe/Fe_3O_4@PPy composites. Pristine PPy exhibited a broad diffuse diffraction peak at 2θ = 25.3°, confirming that the polypyrrole obtained by chemical oxidative polymerization possesses an amorphous non-crystalline structure, which is consistent with conclusions reported in the existing literature[18]. Compared with pure PPy, the Fe/Fe_3O_4@PPy composite retains the broad diffraction peak of PPy at 25.3°, indicating that the amorphous framework of polypyrrole is maintained after compositing. The diffraction peak appearing at 2θ = 35.2° is attributed to the (311) crystal plane of Fe_3O_4, while the sharp diffraction peak at 2θ = 44.6° matches the (110) crystal plane of elemental Fe^0, directly demonstrating that Fe^0 and Fe_3O_4 are successfully loaded into the PPy matrix[19, 20]. The appearance of distinct crystalline phase diffraction signals after the introduction of the iron-based components indicated that the composites formed crystalline phases, with a degree of crystallinity significantly higher than that of pristine amorphous PPy. Combined with the aforementioned FT-IR results, this further confirmed the successful preparation of the Fe/Fe_3O_4@PPy core-shell composites.

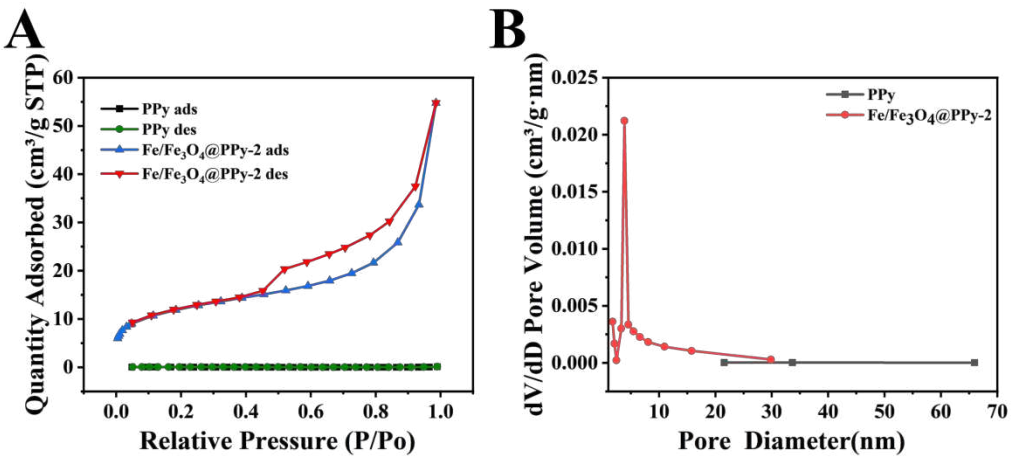

Fig. 3. (A) N_2 adsorption-desorption isotherms of PPy and Fe/Fe_3O_4@PPy-2; (B) pore size distribution curves of PPy and Fe/Fe_3O_4@PPy-2.

The nitrogen adsorption-desorption isotherms and pore size distribution results are shown in Fig. 3. As can be seen from Fig. 3A, pristine PPy exhibited an extremely

low nitrogen adsorption capacity, with a corresponding specific surface area of only 1.6 m^2/g, which is consistent with the dense and smooth surface morphology observed by SEM.[21] The nitrogen adsorption-desorption curve of Fe/Fe_3O_4@PPy-2 indicated that its specific surface area increased to 54.8 m^2/g, which originated from the large number of flower-like porous structures constructed within the polypyrrole matrix by the escape of H_2 during the $NaBH_4$ treatment[22, 23]. The pore size distribution curve (Fig. 3B) showed that Fe/Fe_3O_4@PPy-2 was dominated by mesoporous structures. The abundant mesopores and the enlarged specific surface area can provide sufficient space for adsorption sites, which is favorable for the mass transfer and diffusion of uranium ions within the material.

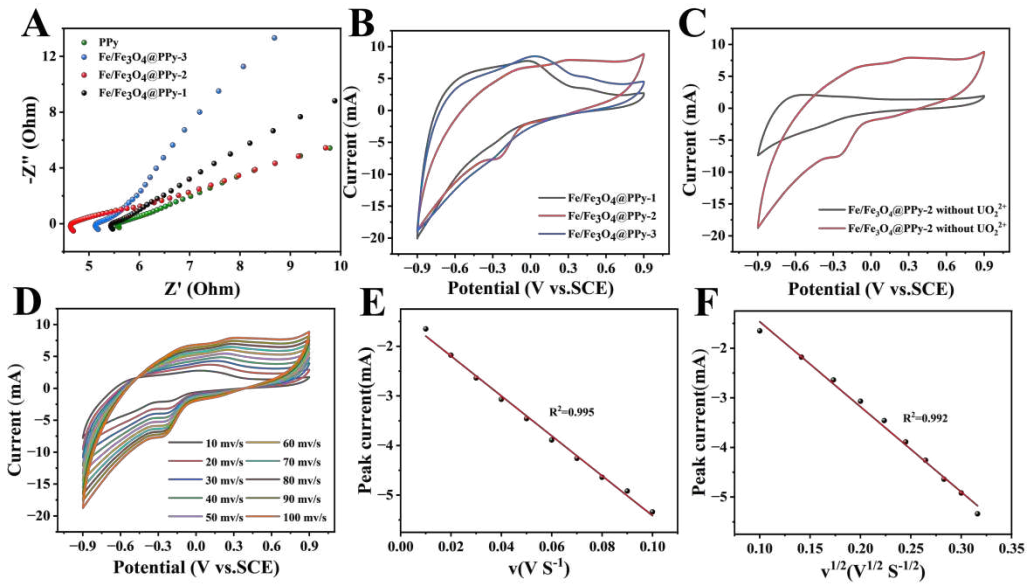

Fig. 4. (A) EIS Nyquist plots of PPy, Fe/Fe_3O_4@PPy-1, Fe/Fe_3O_4@PPy-2, and Fe/Fe_3O_4@PPy-3; (B) CV curves of the three Fe/Fe_3O_4@PPy composites within a voltage window of −0.9 to 0.9 V (pH = 7, C_U = 100 mg L^{-1}); (C) CV curves of Fe/Fe_3O_4@PPy-2 in electrolytes with and without uranium ions; (D) CV curves of Fe/Fe_3O_4@PPy-2 at different scan rates; (E) linear fitting of the peak current versus scan rate for Fe/Fe_3O_4@PPy-2; (F) linear fitting of the peak current versus the square root of the scan rate for Fe/Fe_3O_4@PPy-2.

Electrochemical impedance spectroscopy (EIS) and cyclic voltammetry (CV)

were employed to characterize the electrochemical behavior of the materials. Fig. 4A shows the EIS Nyquist plots of the various samples. Compared with pristine PPy, the capacitive semicircle diameters of all three Fe/Fe_3O_4@PPy composites were markedly reduced, among which Fe/Fe_3O_4@PPy-2 exhibited the smallest semicircle diameter, indicating the lowest charge transfer resistance and the fastest interfacial electron transfer rate. This is consistent with the results that its relatively high specific surface area and porous flower-like structure facilitate electrolyte penetration and the exposure of active sites. Fig. 4B presents the CV curves of the three composites at the same scan rate. All three exhibited a pair of approximately symmetric redox peaks, indicating that the materials possess good electrochemical reversibility. Among them, Fe/Fe_3O_4@PPy-2 had the largest CV enclosed area and the highest corresponding redox peak currents, indicating that it possesses the largest electroactive area and the greatest number of active sites available for reaction. To investigate the electrochemical response of the material toward uranium ions, CV tests were performed in electrolytes with and without uranium ions (Fig. 4C). In the electrolyte system containing uranium ions, the CV curve of Fe/Fe_3O_4@PPy-2 displayed a reduction peak at −0.25 V, and two oxidation peaks were observed at −0.04 V and 0.28 V. The reduction peak at −0.25 V was attributed to the reduction of UO_2^{2+} to lower-valent uranium species mediated by the iron-based active components, while the oxidation peaks at −0.04 V and 0.28 V corresponded to the multi-step oxidation reactions of $Fe^0/Fe^{2+}/Fe^{3+}$ within the material[24, 25].No distinct oxidation peak that could be clearly attributed to the re-oxidation of low-valent uranium was observed, and it is therefore inferred that the oxidation response of uranium was masked by the oxidation signal of the iron component. The reversible valence state transitions of the iron species can continuously supply electrons to the electrode interface and promote the electrochemical reduction of UO_2^{2+}, demonstrating that Fe/Fe_3O_4@PPy-2 can act as an electron mediator to achieve the electroreduction of uranyl ions. Fig. 4D shows the CV curves of Fe/Fe_3O_4@PPy-2 at different scan rates. As the scan rate increased, the redox peak currents increased synchronously, while the peak shapes remained stable. Fig. 4E and 4F show the relationships between the peak current and the scan

rate and the square root of the scan rate, respectively, where the linear fitting of the peak current versus the scan rate corresponds to an adsorption-controlled reaction, while the linear fitting of the peak current versus the square root of the scan rate corresponds to a diffusion-controlled reaction. A comparison of the R^2 values for adsorption control (R^2 = 0.995) and diffusion control (R^2 = 0.992) indicates that the electrochemical reaction is mainly adsorption-controlled.

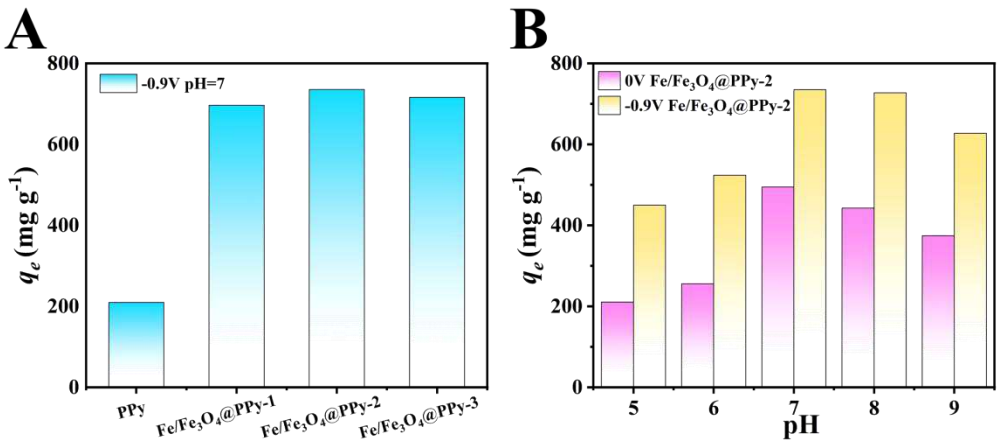

Fig. 5. (A) Adsorption capacities of PPy, Fe/Fe_3O_4@PPy-1, Fe/Fe_3O_4@PPy-2, and Fe/Fe_3O_4@PPy-3 toward UO_2^{2+} at −0.9 V, C_0 = 50 mg L^{-1}, and pH = 7; (B) effect of pH on the electrosorption performance of Fe/Fe_3O_4@PPy-2 in a 50 mg L^{-1} uranium solution at different voltages.

Fig. 5A compares the uranium capture performance of PPy and the series of Fe/Fe_3O_4@PPy composites toward UO_2^{2+} at −0.9 V and pH = 7. Pristine PPy exhibited a relatively weak uranium adsorption capacity under this potential condition. After the introduction of the Fe/Fe_3O_4 active components, the adsorption capacities of all the composites were significantly enhanced, among which Fe/Fe_3O_4@PPy-2 showed the best uranium capture performance. A comparison of the adsorption capacities of the three composites indicates that an appropriate ferric chloride-to-pyrrole ratio is favorable for constructing the flower-like porous structure and providing sufficient electroactive sites, thereby promoting the electroreductive capture of uranyl ions. Based on the comparative U(VI) electrosorption performance

of Fe/Fe_3O_4@PPy-1, Fe/Fe_3O_4@PPy-2, and Fe/Fe_3O_4@PPy-3 (Table S1), Fe/Fe_3O_4@PPy-2 exhibited the highest adsorption capacity and was therefore selected for subsequent mechanistic investigations. Fig. 5B further examined the effect of pH on the uranium adsorption performance of Fe/Fe_3O_4@PPy-2 at 0 V and −0.9 V. At 0 V, the adsorption capacity of the material first increased and then decreased with increasing pH. In an acidic environment, the large amount of H^+ competes with UO_2^{2+} for the coordination sites on the material surface, thereby inhibiting adsorption; under high pH conditions, uranyl readily undergoes hydrolysis to form hydroxyl complexes, which is likewise unfavorable for uranium capture (Figure S1). After applying a cathodic potential of −0.9 V, the uranium capture capacity of the material under the same pH conditions was higher than that of the 0 V system. The electric-field enrichment effect brought about by the strongly negative potential, coupled with electroreductive deposition, greatly enhanced the loading capacity of the material toward uranyl. By comparison, the adsorption capacity of Fe/Fe_3O_4@PPy-2 at 0 V and pH = 4 was weaker than that of pristine PPy at −0.9 V and pH = 7. The reason is that no electric-field enrichment effect exists under the 0 V condition, and the proton competition effect in the acidic medium significantly weakens the uranium capture capacity of the material; in contrast, the strongly cathodic potential of −0.9 V can drive uranyl ions to migrate toward the electrode interface and undergo electroreduction, thereby compensating for the drawback of the low specific surface area of pristine PPy.

Adsorption kinetics studies can elucidate the rate characteristics and mechanism of uranium capture. As shown in Fig. 6A, the uranium capture processes of all samples exhibited a fast adsorption rate in the initial stage, followed by a gradual decrease in rate and eventual approach to adsorption equilibrium. For Fe/Fe_3O_4@PPy-2 at −0.9 V, the abundant active sites on the material surface and the electric-field enrichment effect enabled uranyl ions to rapidly contact the material interface; as the surface active sites were continuously occupied, the mass transfer resistance increased, and the adsorption rate gradually decreased, reaching adsorption equilibrium at approximately 30 min. By comparison, PPy required a relatively longer

time to reach adsorption equilibrium, and its overall uranium capture capacity was far lower than that of Fe/Fe_3O_4@PPy-2. To clarify the adsorption mechanism, the kinetic experimental data were fitted using pseudo-first-order (PFO) and pseudo-second-order (PSO) kinetic models, respectively, and the fitting parameters are listed inTable S2.At −0.9 V, the coefficient of determination obtained from the pseudo-second-order kinetic model for Fe/Fe_3O_4@PPy-2 (R^2 = 0.997) was higher than that from the pseudo-first-order kinetic model (R^2 = 0.992). In addition, the theoretical equilibrium adsorption capacity calculated from the pseudo-second-order kinetic model ($q_2$cal) was 741.16 mg·g^{-1}, which is close to the experimental value. A comparison of the rate constants shows that the pseudo-second-order rate constant k_2 of Fe/Fe_3O_4@PPy-2 at −0.9 V (1.08×10^{-3} g mg^{-1} min^{-1}) was lower than that of pristine PPy (1.52×10^{-3} g mg^{-1} min^{-1}), whereas the corresponding equilibrium adsorption capacity increased by 254%. This indicates that the interpretation of the rate constant needs to be comprehensively analyzed in combination with the adsorption capacity. The flower-like porous structure constructed in the Fe/Fe_3O_4@PPy composite introduces a large number of active sites available for immobilizing uranium species, greatly enhancing the uranium capture capacity.

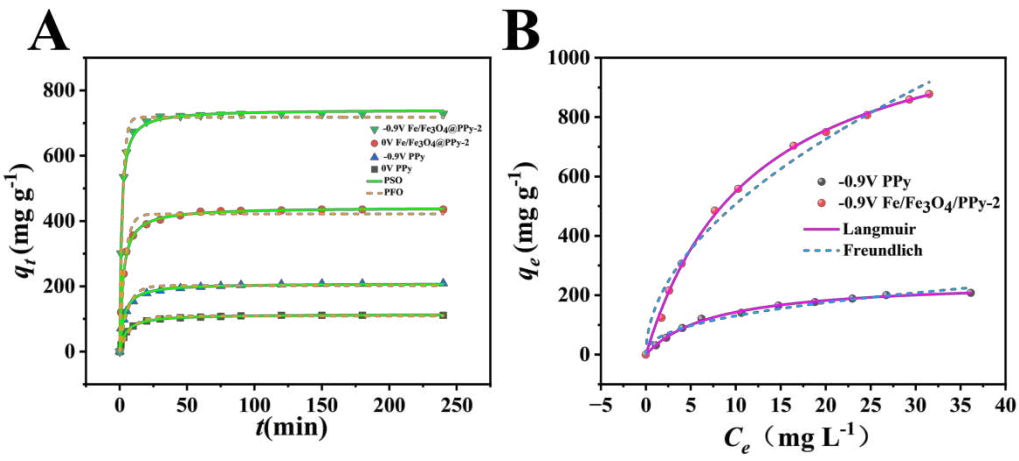

Fig. 6. (A) Kinetic curves of uranium ion adsorption by PPy and Fe/Fe_3O_4@PPy-2 at different voltages (C_0 = 50 mg L^{-1}, pH = 7); (B) adsorption isotherms of uranium ions by PPy and Fe/Fe_3O_4@PPy-2 at −0.9 V (C_0 = 10–80 mg L^{-1}, pH = 7, T = 25°C, t = 240 min).

The interaction between the adsorbent and the adsorbate at equilibrium was described by studying the adsorption isotherms. As shown in Fig. 6B, the adsorption capacity of Fe/Fe_3O_4@PPy-2 increased with increasing initial U (VI) concentration and eventually reached a plateau. The experimental data were fitted using the Langmuir and Freundlich isotherm models, respectively.[26, 27]

The fitting parameters are listed in Table S3. For Fe/Fe_3O_4@PPy-2, the correlation coefficient obtained from the Langmuir model (R^2 = 0.999) was higher than that from the Freundlich model (R^2 = 0.983), indicating that the adsorption of U(VI) on Fe/Fe_3O_4@PPy-2 mainly follows a homogeneous monolayer adsorption process occurring on a surface with a finite number of active sites. According to the Langmuir model, the theoretical maximum adsorption capacity (q_m) of Fe/Fe_3O_4@PPy-2 for U(VI) was 1208.60 $mg \cdot g^{-1}$, which is much higher than that of PPy (251.19 $mg \cdot g^{-1}$). This result confirms the important contribution of the flower-like porous structure of the nanocomposite to its U(VI) adsorption performance.[28] Although the Langmuir affinity constant K_L of Fe/Fe_3O_4@PPy-2 was 0.0835 $L \cdot mg^{-1}$, which is lower than that of PPy (0.132 $L \cdot mg^{-1}$), the Freundlich constant K_F of Fe/Fe_3O_4@PPy-2 was 154.41, far higher than that of PPy (49.11), further indicating that Fe/Fe_3O_4@PPy-2 possesses a higher adsorption capacity. In summary, both the Langmuir and Freundlich parameters indicate that the introduction of Fe and Fe_3O_4 greatly enhances the uranium adsorption performance of the nanocomposite.[29]

To benchmark the performance of Fe/Fe_3O_4@PPy-2, its Langmuir maximum capacity was compared with those of selected electrochemical U(VI) adsorbents.As summarized in Table 1, Fe/Fe_3O_4@PPy-2 exhibits a competitive U(VI) adsorption capacity compared with previously reported electrochemical adsorbents.

Table 1 Comparison of U(VI) adsorption performance of Fe/Fe_3O_4@PPy with selected electrochemical uranium adsorbents

Adsorbents	exp conditions	pH	q_{max}（mg g^{-1}）	Reference
CS/PA-PPy	1.2V	5	799.3	[30]

SC/MoS_2/PPy	−0.9V	4.5	300.7	[31]
SA-FeOOH	1.2V	4	709.4	[32]
α-Fe_2O_3	1.2V	4	490.2	[33]
PA@MIL-53(Fe)-NH_2	−0.9V	5	1128.0	[34]
NTP	−0.9V	4	271.5	[35]
Fe/Fe_3O_4@PPy-2	−0.9V	7	1208.6	This work

q_{max}: The maximum adsorption capacity of the Langmuir isotherm

Note: CS/PA-PPy: Chitosan/Phytic Acid-Polypyrrole

SC/MoS_2/PPy: Sugar-derived Carbon/Molybdenum Disulfide/Polypyrrole

SA-FeOOH: Sulfonic acid-decorated FeOOH

PA@MIL-53(Fe)-NH_2: Phytic acid-functionalized MIL-53(Fe)-NH_2

NTP: Polypyrrole modified N-doped chitosan-derived carbon/nano-TiO_2

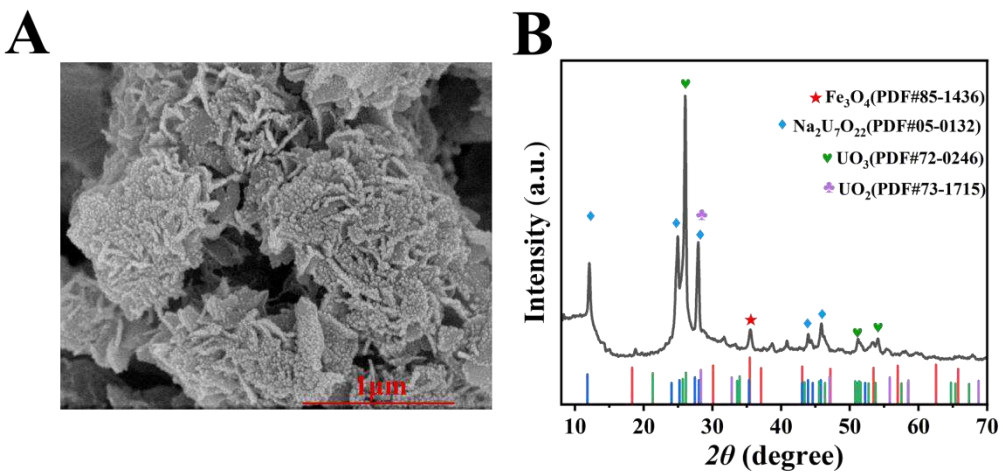

Fig. 7 (A) SEM image of Fe/Fe_3O_4@PPy-2 after U(VI) adsorption;(B)XRD pattern of Fe/Fe_3O_4@PPy-2 after electrosorption.

To further analyze the surface species after electrosorption of U(VI), the SEM image after adsorption is shown in Fig. 7A. The SEM image reveals that Fe/Fe_3O_4@PPy-2 still maintained its original flower-like porous structure after the electrosorption reaction, and numerous granular deposits were uniformly distributed on the material surface, indicating that uranium species were successfully deposited on the adsorbent surface.The above results intuitively confirm that uranyl ions were

effectively enriched and immobilized on the composite surface during the electrosorption process.[36] To investigate the mechanism of uranium adsorption, the electrode surface was characterized, as shown in Fig. 7B. In the XRD pattern, the characteristic diffraction peaks of Fe_3O_4 (PDF#85-1436), $Na_2U_7O_{22}$ (PDF#05-0132), UO_3 (PDF#72-0246), and UO_2 (PDF#73-1715) were simultaneously observed.[24, 37] Based on these results, a series of possible chemical reactions occurring during the electrosorption process can be inferred:

(1) UO_2 originates from the redox reaction between UO_2^{2+} and iron during the electrosorption process, as well as from the electrochemical reduction of UO_2^{2+}.

$UO_2^{2+} + Fe^0 \rightarrow UO_2(s) + Fe^{2+}$ $\quad$ $Fe^{2+} + UO_2^{2+} \rightarrow Fe^{3+} + UO_2^{+}$

$UO_2^{2+} + e^- \rightarrow UO_2^{+}$ $\quad$ $2UO_2^{+} \rightarrow UO_2^{2+} + UO_2$（s）

(2) Fe_3O_4 originates from the reaction between Fe^{2+} and Fe^{3+} generated by the redox reaction with UO_2^{2+} in (1).

$Fe^{2+} + 2Fe^{3+} + 8OH^- \rightarrow Fe_3O_4(s) + 4H_2O$

(3) UO_3 originates from the reaction of electrosorbed UO_2^{2+} with water.

$UO_2^{2+} + H_2O \rightarrow UO_3(s) + 2H^+$

(4) $Na_2U_7O_{22}$ originates from the reaction between Na^+ in solution and UO_2^{2+} during pH adjustment.

$7UO_2^{2+} + 2Na^+ + 22OH^- \rightarrow Na_2U_7O_{22}(s) + 11H_2O$

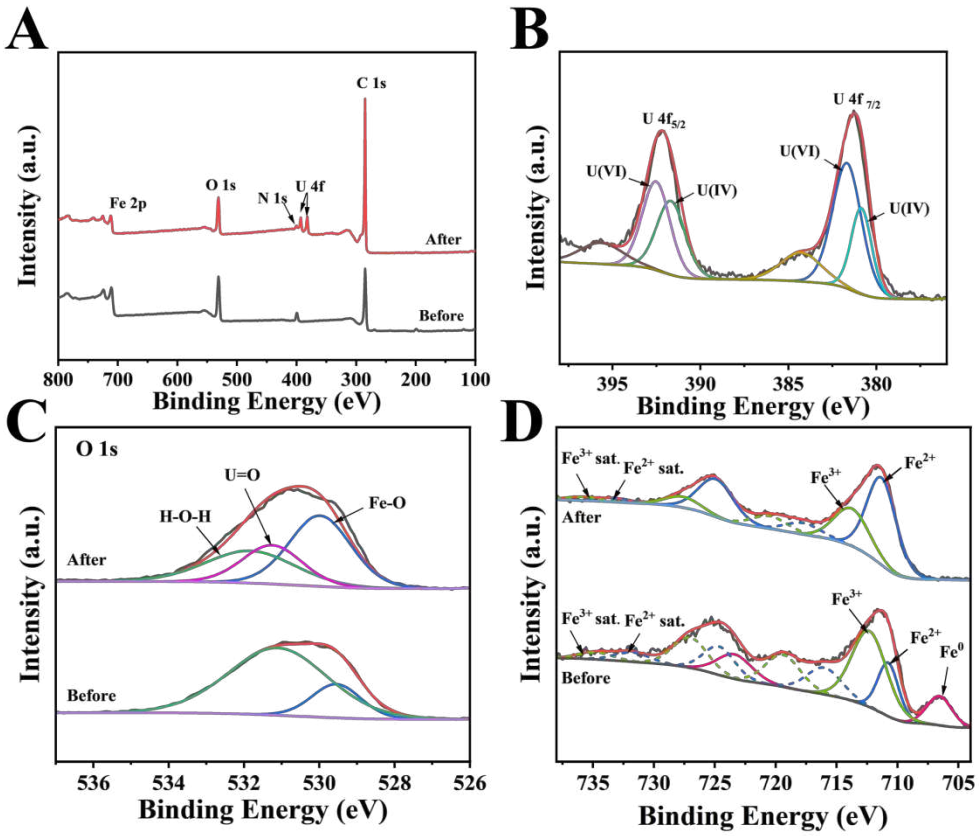

Fig. 8. (A) XPS spectra of Fe/Fe_3O_4@PPy-2 before and after adsorption; (B) high-resolution U 4f spectrum after adsorption; (C) high-resolution O 1s spectra before and after adsorption; (D) high-resolution Fe 2p spectra before and after adsorption.

To further reveal the valence state evolution of interfacial elements and the underlying mechanism during the electrosorption of U(VI), XPS characterization was performed on Fe/Fe_3O_4@PPy-2 samples before and after adsorption, and the results are shown in Fig. 8. Fig. 8A presents the XPS survey spectra before and after adsorption. Compared with the sample before adsorption, the spectrum after electrosorption exhibited distinct characteristic signals in the U 4f region, directly confirming that uranium species were successfully loaded onto the surface of the Fe/Fe_3O_4@PPy-2 composite.

Figure 8B shows the high-resolution U 4f spectrum. The U $4f_{7/2}$ and U $4f_{5/2}$ orbitals correspond to peaks at 381.28 and 392.18 eV, respectively. The fitted peaks of the U $4f_{7/2}$ orbital at 380.85 eV and 381.67 eV are assigned to U(IV) and U(VI),

respectively; the fitted peaks of the U $4f_{5/2}$ orbital at 391.68 eV and 392.52 eV correspond to U(IV) and U(VI), respectively.[25, 38] Based on these data, the XPS and calculation results yield a peak area ratio of U(IV) to U(VI) on the material surface of approximately 105:167. These results indicate that elemental iron underwent a redox reaction with part of the U(VI), while the remaining U(VI) was bound to the active sites of the material through coordination.

The high-resolution O 1s spectrum is shown in Figure 8C. Before adsorption, the O1s spectrum exhibited characteristic peaks at 529.55 eV and 531.10 eV, corresponding to Fe-O bonds and H-O-H, respectively. After electrosorption, the O 1s spectrum can be fitted into three characteristic peaks at 529.98 eV (Fe–O), 531.25 eV (H–O–H), and 531.83 eV (U=O).[39, 40] The newly appearing U=O characteristic peak demonstrates that uranyl ions undergo interfacial coordination interactions with oxygen-containing groups on the material surface, further confirming the successful immobilization of uranium species.[41]

The high-resolution Fe 2p spectrum is shown in Figure 8D. Before adsorption, a characteristic peak assignable to Fe^0 was observed at 706.56 eV in the Fe 2p spectrum, along with Fe^{2+} (710.76 and 724.65 eV), Fe^{3+} (712.31 and 727.02 eV), and their corresponding satellite peaks, indicating that the pristine material contained a composite iron component of Fe/Fe_3O_4. After electrosorption, the characteristic peak of Fe^0 at 706.56 eV disappeared completely, with only Fe^{2+}, Fe^{3+}, and their satellite peaks remaining.[42-44] This demonstrates that zero-valent iron in the material was oxidized as an electron donor during the electrosorption process, providing electrons for the reduction of UO_2^{2+}.

In summary, the electrocapture mechanism of Fe/Fe_3O_4@PPy-2 toward U(VI) can be summarized as follows: the unique flower-like porous structure of the material provides abundant reactive sites; under an applied electric field, UO_2^{2+} is enriched at the material interface, where one portion of UO_2^{2+} is immobilized through coordination with oxygen-containing functional groups on the material surface, while another portion accepts electrons provided by Fe^0 and the cathodic electric field and is reduced to U(IV), forming UO_2 precipitates. The synergistic effect of coordination

enrichment and electrochemical reduction jointly enables efficient uranium removal.[3, 45]

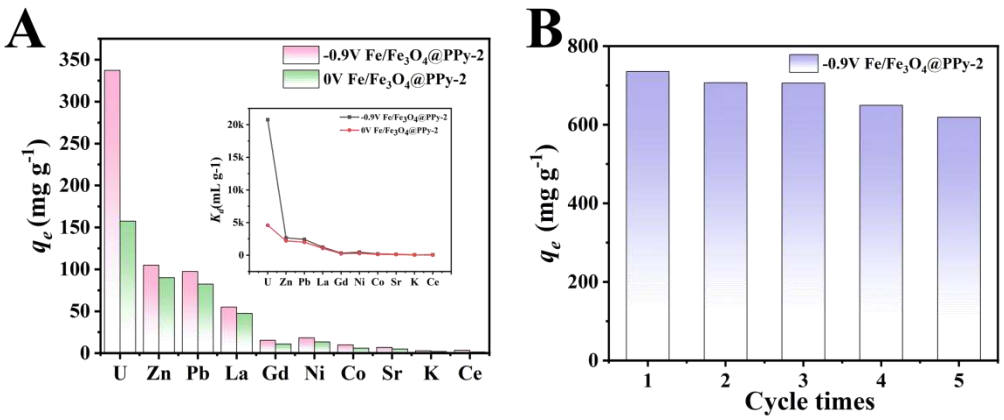

Figure 9. (A) Adsorption capacities (q_e) of Fe/Fe_3O_4@PPy-2 for uranium and various coexisting ions at applied potentials of −0.9 V and 0 V; the inset shows the distribution coefficients (K_d) for each ion. (B) Cycling performance of Fe/Fe_3O_4@PPy-2 over five consecutive electrosorption-desorption cycles at an applied potential of −0.9V.

The selectivity of Fe/Fe_3O_4@PPy-2 was evaluated in a complex solution containing UO_2^{2+} and various competing ions (Zn^{2+}, Cu^{2+}, Co^{2+}, etc.). As shown in Figure 9A, the Fe/Fe_3O_4@PPy-2 electrode exhibited significant selectivity for uranium at −0.9 V, with an electrosorption capacity for UO_2^{2+} reaching 337.50 mg g^{-1}, which was significantly higher than the adsorption capacity at 0 V (157.50 mg g^{-1}). The distribution coefficient (K_d) of the electrode for uranium was also as high as 2.08×10^4 mL g^{-1}. The excellent performance of Fe/Fe_3O_4@PPy-2 in the selective adsorption of U(VI) is mainly attributed to the interactions between uranyl ions and Fe/Fe_3O_4@PPy-2. The amino groups on PPy and the oxygen atoms in Fe_3O_4 in the Fe/Fe_3O_4@PPy-2 electrode can coordinate with uranyl ions.[46]

The reusability of the electrode was evaluated through five consecutive electrosorption-desorption cycles (Figure 9B). The Fe/Fe_3O_4@PPy-2 electrode exhibited excellent cycling stability, with only a slight decrease in uranium

electrosorption capacity after five cycles, still retaining 84.22% of the initial capacity. This excellent performance is closely related to the desorption method: reverse voltage was used for desorption during the cycles rather than acidic or sodium salt solutions. The reverse voltage reverses the electric field, causing the electrode surface to switch from negative polarization to positive polarization. The originally electrostatically attracted uranyl ions and the uranium species deposited on the surface migrate out due to electrostatic repulsion. Meanwhile, the positively polarized environment can re-oxidize part of U(IV) to U(VI) into the solution, achieving efficient desorption.[47, 48] This method does not introduce additional chemical etching agents, thereby avoiding the dissolution loss of Fe^0 and Fe_3O_4 active components under acidic conditions, and also avoiding competitive adsorption and secondary pollution caused by the introduction of high-concentration Na^+. Thus, while maintaining desorption efficiency, it maximally protects the structural integrity and active sites of the electrode, which is the key reason why the capacity still remains at 84.22% after five cycles.

4 Conclusion

In this study, Fe/Fe_3O_4@PPy core–shell nanocomposites were successfully fabricated through an oxidative polymerization–in situ reduction approach and applied for electrochemical capture of U(VI). The optimized Fe/Fe_3O_4@PPy-2 electrode exhibited high uranium removal performance, achieving an experimental capacity of 735.57 mg g^{-1} and a maximum Langmuir capacity of 1208.6 mg g^{-1} at neutral pH. The composite also demonstrated excellent selectivity in multicomponent systems and retained 84.22% of its initial capacity after five regeneration cycles.The enhanced uranium capture performance was attributed to the synergistic contribution of the porous PPy-based core–shell structure and the redox-active iron species. The PPy/Fe_3O_4 interface promoted uranium enrichment through coordination interactions, while Fe^0 served as an electron donor to induce partial reduction of U(VI) into insoluble U(IV) species. The combination of electrochemical enrichment and reductive immobilization enables efficient and stable uranium removal. These findings highlight the potential of iron-based conducting polymer composites for the

sustainable recovery of uranium from dilute aqueous systems.

Conflicts of interest

There are no conflicts to declare.

Data availability

The data supporting the findings of this study are presented in the main article and the accompanying Supporting Information.

Acknowledgments

The authors are grateful for the financial support of the National Natural Science Foundation of China (No. 22466002), the Natural Science Foundation of Jiangxi Province (No. 20242BAB26061, 20262BAC240094).

References

[1] L. Loreggian, A. Novotny, S. L. Bretagne, B. Bartova, Y. Wang, R. Bernier-Latmani, Effect of aging on the stability of microbially reduced uranium in natural sediment, Environmental Science & Technology. 54 (2020) 613–20.

[2] M. Su, S. Wang, J. Pan, M. Chen, C. Shen, Y. Lai, J. Zhao, J. Yang, D. Chen, Y. Zhou. Immobilization of soluble U(VI) from simulated wastewater into a stable mineral: V_2O_5-induced crystallization of uvanite for uranium remediation, Environmental Research. 291 (2026) 123533.

[3] M. Xiao, B. Huang, T. Jin, C. Yan, Z. Liu, Y. Qian, Synergistic phosphoryl group and sulfur vacancy engineering on MoS_2 nanosheets for highly efficient electrochemical uranium extraction. ***Desalination*** 618 (2026) 119444.

[4] L. Xie, T. Jin, C. Yan, C. Wang, B. Huang, Y. Qian. Efficient extraction of U(VI) from uranium-containing wastewater over a wide pH range using sulfonate-rich electrode materials, Environmental Research. 309 (2026) 125828.

[5] T. Lin, T. Chen, C. Jiao, H. Zhang, K. Hou, H. Jin, Y. Liu, W. Zhu, R. He. Ion pair sites for efficient electrochemical extraction of uranium in real nuclear wastewater, Nature Communications. 15 (2024) 4149.

[6] Y. Hua, D. Li, J. Zou, W. Wang, X. Wu, X. Zhang, Q. Liu, G. Zhao, M. Li, W.-X. Zhang, J. Yang. Evolutional solid phase and solid-liquid interface uranium immobilization mechanisms by nanoscale zero-valent iron and enhanced uranium stability control strategy, Chemical Engineering Journal. 453 (2023) 139924.

[7] Y.-P. Sun, X.-Q. Li, J. Cao, W.-X. Zhang, H. P. Wang. Characterization of zero-valent iron nanoparticles, Advances in Colloid and Interface Science. 120(2006) 47–56.

[8] Y. Li, X. Zhou, A. Long, S. Huang, J. Liu, Y. Shen, L. Sun, S. Wang, F. Liu. Synergistic enhancement of Cr(VI) removal by nano zero-valent iron/polypyrrole composite lignin-derived sulfur self-doped hierarchical porous carbon: adsorption, reduction, and immobilization, Separation and Purification Technology, 394 (2026) 137464.

[9] Y. Chen, Z. Lin, R. Hao, H. Xu, C. Huang. Rapid adsorption and reductive degradation of Naphthol Green B from aqueous solution by polypyrrole/attapulgite composites supported nanoscale zero-valent iron, Journal of Hazardous Materials. 371 (2019) 8–17.

[10] R. Peymanfar, F. Norouzi, S. Javanshir. A novel approach to prepare one-pot Fe/PPy nanocomposite and evaluation of its microwave, magnetic, and optical performance, Materials Research Express. 6 (2019) 035024.

[11] Y. Hua, W. Wang, N. Hu, T. Gu, L. Ling, W.-X. Zhang. Enrichment of uranium from wastewater with nanoscale zero-valent iron (nZVI), Environmental Science: Nano. 8 (2021) 666–74.

[12] I. B. Qader, H. K. Ismail, H. F. Alesary, J. H. Kareem, Y. T. Maaroof, S. Barton. Electrochemical sensor based on polypyrrole/triiron tetraoxide (PPy/Fe_3O_4) nanocomposite deposited from a deep eutectic solvent for voltammetric determination of procaine hydrochloride in pharmaceutical formulations,Journal of Electroanalytical Chemistry. 951 (2023) 117943.

[13] M. Ma, Y. Bi, Z. Jiao, J. Yue, Z. Liao, Y. Wang, Y. Ma, W. Huang. Facile fabrication of metal–organic framework derived Fe/Fe_3O_4/FeN/N-doped carbon

composites coated with PPy for superior microwave absorption, Journal of Colloid and Interface Science. 608 (2022) 525–35.

[14] A. Tavousi, E. Ahmadi, L. Mohammadi-Behzad, V. Riahifar, F. Maghemi. Sensitive electrochemical sensor using polypyrrole-coated Fe_3O_4 core-shell nanoparticles/multiwall carbon nanotubes modified graphite electrode for atorvastatin analysis, Microchemical Journal. 158 (2020) 105159.

[15] D. Zhang, H. Chen, X. Zhou, D. Wang, Y. Jin, S. Yu. In-situ polymerization of metal organic frameworks-derived $ZnCo_2O_4$/polypyrrole nanofilm on QCM electrodes for ultra-highly sensitive humidity sensing application,Sensors and Actuators A: Physical. 295 (2019) 687–95.

[16] M. Afzali, A. Mostafavi, Z. Afzali, T. Shamspur. Designing a rapid and selective electrochemical nanosensor based on molecularly imprinted polymer on the Fe_3O_4/MoS_2/glassy carbon electrode for detection of immunomodulatory drug pomalidomide, Microchemical Journal. 164 (2021) 106039.

[17] B. A. M. Babakir, L. I. Abd Ali, H. K. Ismail.Rapid removal of anionic organic dye from contaminated water using a poly(3-aminobenzoic acid/graphene oxide/cobalt ferrite) nanocomposite low-cost adsorbent via adsorption techniques, Arabian Journal of Chemistry.15 (2020) 104318.

[18] T. Gayathri, T. Magray, B. Kavitha, M. Nirmala, P. Sarawade. Tuning NiO/RGO nano-composite electrodes: the synergistic role of polyaniline and polypyrrole in structure, morphology, and charge storage dynamics in supercapacitors, Journal of Energy Storage 162 (2026) 122061.

[19] L. S. Zhong, J. S. Hu, H. P. Liang, A. M. Cao, W. G. Song, L. J. Wan. Self-assembled 3D flowerlike iron oxide nanostructures and their application in water treatment, Advanced Materials. 18(2006) 2426–31.

[20] Z. Yang, X. Ma, C. Shan, X. Guan, W. Zhang, L. Lv, B. Pan. Activation of zero-valent iron through ball-milling synthesis of hybrid Fe^0/Fe_3O_4/$FeCl_2$ microcomposite for enhanced nitrobenzene reduction, Journal of Hazardous Materials. 368 (2019) 698–704.

[21] Y. Cheng, J. Zhao, G. Wang. Synthesis of polypyrrole nanoparticles by

microemulsion polymerization for photocatalysis, Journal of Wuhan University of Technology Materials Science Edition. 28(2013) 787–92.

[22] A. Mollahosseini, A. Khadir, J. Saeidian. Core–shell polypyrrole/Fe_3O_4 nanocomposite as sorbent for magnetic dispersive solid-phase extraction of Al^{3+} ions from solutions: investigation of the operational parameters, Journal of Water Process Engineering. 29 (2019) 100795.

[23] T. Zhou, Q. Liang, X. Zhou, H. Luo, W. Chen. Enhanced removal of toxic hexavalent chromium from aqueous solution by magnetic Zr-MOF@polypyrrole: performance and mechanism, Environmental Science and Pollution Research International. 28(2021) 13084–96.

[24] D. Guo, C. Yan, B. Huang, T. Jin, Z. Liu, Y. Qian. Combining electrosorption and electrochemical reduction mechanisms for uranium removal using 1,2,3,4-butane tetracarboxylic acid-modified MIL-101: an in-depth exploration of uranyl–adsorbent interactions, Inorganic Chemistry. 64(2025) 1777–87.

[25] S. Yang, C. Yan, B. Huang, T. Jin, D. Guo, M. Xiao, Y. Qian. PBTCA-modified self-crosslinked chitosan gels for efficient electrosorption of uranium from wastewater, Desalination. 612 (2025) 118984.

[26] M. A. Al-Ghouti, D. A. Da'ana. Guidelines for the use and interpretation of adsorption isotherm models: a review, Journal of Hazardous Materials. 393 (2020) 122383.

[27] X. Chen, M. F. Hossain, C. Duan, J. Lu, Y. F. Tsang, M. S. Islam, Y. Zhou. Isotherm models for adsorption of heavy metals from water: a review, Chemosphere. 307 (2022) 135545.

[28] R. Ma, L. Yin, L. Li, S. Zhang, T. Wen, C. Zhang, X. Wang, Z. Chen, T. Hayat, X. Wang. Comparative investigation of Fe_2O_3 and $Fe_{1-x}S$ nanostructures for uranium decontamination, ACS Applied Nano Materials. 1(2018) 5543–52.

[29] J. Wang, Q. Hu, R. Jiao, J. Li. Magnetically separable MXene/Fe_3O_4 electrode for uranium (VI) deionization, Journal of Environmental Chemical Engineering. 13(2025) 117006.

[30] X. Zhao, D. Chen, M. Shi, R. Zhao. Anchoring chitosan/phytic acid complexes

on polypyrrole nanotubes as capacitive deionization electrodes for uranium capture from wastewater, International Journal of Biological Macromolecules. 270 (2024) 132491.

[31] H. Shehzad, J. Chen, M. T. Shuang, Z. Liu, L. Zhou, Y. Wang, Z. H. Farooqi, E. Ahmed, A. Sharif, A. Irfan, J. Ouyang, Z. Feng. Evaluation of templated N/P co-doped hierarchical mesoporous biocarbon/2D-molybdenum disulfide /polypyrrole composite as a supercapacitor electrode for U(VI) electrosorption, Separation and Purification Technology. 329 (2024) 125226.

[32] R. Jiao, Z. Chen, S. Zeng, D. Wang, J. Li. Electrosorption of uranium (VI) by sulfonic acid-decorated FeOOH nanorods, Journal of Environmental Chemical Engineering. 11(2023) 111275.

[33] H. Zhou, R. Jiao, X. Ma, J. Han, S. Zeng, Y. Mi. High-efficiency sea urchin-like α-Fe_2O_3 nanoflower cathode for electrosorption of uranium(VI), Journal of Environmental Chemical Engineering. 14(2026) 122709.

[34] T. Jin, C. Qin, J. Luo, H. Jiang, C. Yan, L.-L. Liu. Phytic acid-functionalized MIL-53(Fe)-NH_2 for electro-assisted capture and immobilization of U(VI) from aqueous solution, Inorganic Chemistry Communications. 192 (2026) 117422.

[35] L. Zhou, D. Liu, G. Xia, J. Li, J. Ouyang, Z. Yang, A. M. Elgarahy, K. Z. Elwakeel. In situ nitrogen-doped honeycomb-like chitosan-derived carbon/TiO_2 aerogel modified with conductive polypyrrole for efficient electrosorption of U(VI), Journal of Environmental Chemical Engineering. 13(2025) 118952.

[36] Y. Yu, Z.-Y. Zhu, H. Ye, G.-T. Chen, M.-B. Wu, X. Kong, J. Militky, J. Yao. Lysozyme@Fe_3O_4 composite adsorbents with enhanced adsorption rates and uranium/vanadium selectivity by photothermal property, Composites Communications. 36 (2022) 101364.

[37] Y. Liao, R. Lei, X. Weng, C. Yan, J. Fu, G. Wei, C. Zhang, M. Wang, H. Wan. Uranium capture by a layered 2D/2D niobium phosphate/holey graphene architecture via an electro-adsorption and electrocatalytic reduction coupling process, Journal of Hazardous Materials. 442 (2023) 130054.

[38] J. Huang, Z. Liu, D. Huang, T. Jin, Y. Qian. Efficient removal of uranium (VI)

with a phytic acid-doped polypyrrole/carbon felt electrode using double potential step technique, Journal of Hazardous Materials. 433 (2022) 128775.

[39] Y. Hua, W. Wang, N. Hu, T. Gu, L. Ling, W.-X. Zhang. Enrichment of uranium from wastewater with nanoscale zero-valent iron (nZVI), Environmental Science: Nano. 374 (2021) 186372.

[40] H. Zhang, Y. Ruan, A. Liang, K. Shih, Z. Diao, M. Su, L. A. Hou, D. Chen, H. Lu, L. Kong. Carbothermal reduction for preparing nZVI/BC to extract uranium: insight into the iron species dependent uranium adsorption behavior, Journal of Cleaner Production. 239 (2019) 117873.

[41] J. Huang, Z. Liu, D. Huang, T. Jin, Y. Qian, Electrochemical deposition of uranium oxide with an electrocatalytically active electrode using double potential step technique. Chinese Chemical Letters. 33 (2022) 3762–3766.

[42] S. Tsarev, R. N. Collins, A. Fahy, T. D. Waite. Reduced uranium phases produced from anaerobic reaction with manoscale zerovalent iron, Environmental Science & Technology. 50(2016) 2595–601.

[43] R. Wang, M. Li, T. Liu, X. Li, L. Zhou, L. Tang, C. Gong, X. Gong, K. Yu, N. Li, W. Zhu, T. Chen. Encapsulating carbon-coated nano zero-valent iron particles with biomass-derived carbon aerogel for efficient uranium extraction from uranium-containing wastewater, Journal of Cleaner Production. 364 (2022) 132654.

[44] X. Ye, J. Tian, P. Chen, L.-A. Ma, J. Chen, Q Wang. Polypyrrole modified MIL-101-Fe-derived Fe/Fe_3O_4@C composites for high-performance microwave absorber, Journal of Materials Research and Technology. 31 (2024) 2961–71.

[45] Y. Cai, P. Li, Q. Yuan, J. Zhao, P. Tsiakaras. Efficient and selective uranium electrochemical extraction over flexibly engineered bi-functional Polypyrole@$MoSe_2$@MXene, Chemical Engineering Journal. 507 (2025) 160496.

[46] Y. Zhang, J. B. Fein, Y. Li, Q. Yu, B. Zu, C. Zheng. U(VI) adsorption to Fe_3O_4 nanoparticles coated with lignite humic acid: experimental measurements and

surface complexation modeling, Colloids and Surfaces A: Physicochemical and Engineering Aspects. 614 (2021) 126150.

[47] R. He, Y. Kong, Y. Li, X. Tang, Y. Liu, T. Duan, W. Zhu. Rapid electrochemical uranium extraction from real seawater via the intermediate of vacancy-trapped isolated uranyl, Inorganic Chemistry. 64(2025) 2371–8.

[48] F. Yang, P. Ding, M. Wang, Y. Liu, X. Zhang, Y. Yuan, Y. Sun, X. Guan. Enhanced electrochemical uranium extraction by three-dimensional zero-valent iron aerogels via dynamic Fe(II)/Fe(III) cycling, Chemical Engineering Journal. 542 (2026) 178197.

Supplementary Files

This is a list of supplementary files associated with this preprint. Click to download.

- SIFu10.22docx.docx